

# AIRS deconvolution and the translation of AIRS to CrIS radiances with applications for the IR climate record

\*\*\*\* DRAFT \*\*\*\*

Howard E. Motteler  
L. Larrabee Strow

UMBC Atmospheric Spectroscopy Lab  
Joint Center for Earth Systems Technology

November 21, 2017

## Abstract

Spectra of the earth’s thermal emission as measured by the AIRS, CrIS, and IASI hyper-spectral sounders is a significant part of the long term climate record. These instruments have broadly similar spatial sampling, spectral resolution, and band spans. However the channel spectral response functions differ in detail, leading to significant differences in observed spectra. To address this we translate channel radiances from one sounder to another, including simulation of the response functions of the translation target. We make regular use of such translations from AIRS to CrIS and IASI to CrIS, and have implemented and tested IASI to AIRS and CrIS to AIRS translations as well. Our translation from AIRS to CrIS has some novel features. AIRS is a grating spectrometer with a distinct response function for each channel, while CrIS is a Michelson interferometer with a sinc response function after calibration and corrections. We use our detailed knowledge of the AIRS spectral response functions to deconvolve AIRS channel radiances to a resolution enhanced intermediate representation. This is reconvolved to CrIS or other instrument specifications. The resulting translation is shown to be more accurate than interpolation or conventional regression.

## 1 Introduction

Spectra of the earth’s thermal emission as measured by the AIRS [1], CrIS [2, 11], and IASI [4] hyperspectral infrared sounders is a significant part of the long term climate record. Such measurements began with AIRS in 2002 and should continue for the foreseeable future, given

their important role in numerical weather prediction. These sounders are in sun-synchronous near-polar orbits, with broadly similar spatial sampling, spectral resolution, and spectral band spans. However the spectral response functions vary in detail, and this can lead to significant differences in observed spectra.

For applications such as calibration and validation, retrievals, and the construction of a long term climate record we would like to work with single set of spectral response functions. This can be done by translating channel radiances from one sounder to another, including simulation of the response functions of the translation target. We make regular use of translations from AIRS to CrIS and IASI to CrIS, and have implemented and tested IASI to AIRS and CrIS to AIRS translations as well. The translations from IASI includes deapodization (a form of deconvolution) before reconvolution to the translation target, and work very well. Ranking these translations by accuracy in comparison with calculated reference truth, we have IASI to CrIS, IASI to AIRS, AIRS to CrIS, and finally CrIS to AIRS [7]. But aside from the AIRS to CrIS translation the methods used are for the most part conventional.

Our translation from AIRS to CrIS has some novel features. AIRS is a grating spectrometer with a distinct response function for each channel determined by the focal plane geometry, while CrIS is a Michelson interferometer with a sinc response function after calibration and corrections. In section 2 we show how to take advantage of our detailed knowledge of the AIRS spectral response functions (SRFs) and their overlap to deconvolve channel radiances to a resolution-enhanced intermediate representation, typically a  $0.1 \text{ cm}^{-1}$  grid,

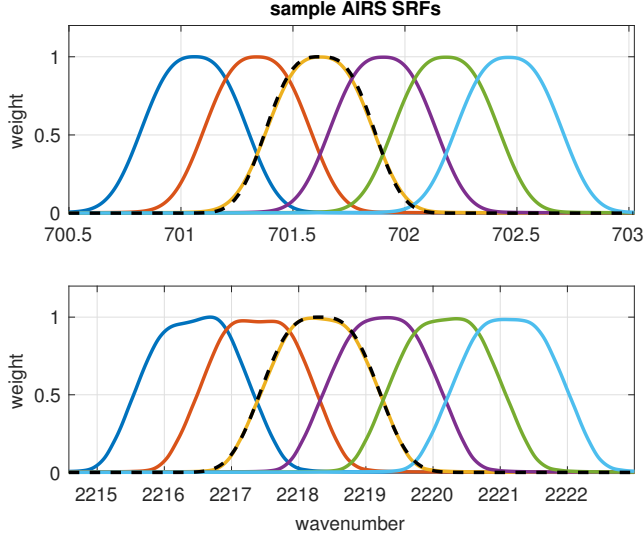


Figure 1: sample AIRS spectral response functions from the low and high ends of the band. The dashed line is a generalized Gaussian function.

the approximate resolution of the tabulated AIRS SRFs. This intermediate representation can then be reconvolved to an alternate instrument specification. Section 3 gives details and validation tests for an AIRS to CrIS translation, and section 4 for translation from AIRS to an idealized grating model. Both translations can be further improved with a statistical correction. In section 5 we consider conventional and principal component regression for an AIRS to CrIS translation, and compare this with our deconvolution-based translation.

## 2 AIRS Deconvolution

The AIRS spectral response functions model channel response as a function of frequency and associate channels with nominal center frequencies. Each AIRS channel  $i$  has an associated spectral response function or SRF  $\sigma_i(v)$  such that the channel radiance  $c_i = \int \sigma_i(v)r(v) dv$ , where  $r$  is radiance at frequency  $v$ . The center or peak of  $\sigma_i$  is the nominal channel frequency.

Figure 1 shows typical AIRS SRFs from the low and high ends of the band. Note the significant overlap in the wings. This can allow for a deconvolution to recover resolution beyond that of the response functions considered individually. The SRFs are not necessarily symmetrical, especially at the high end of the band. The dashed line on top of the third SRF in each group is a fit for a generalized Gaussian, which we consider in more detail later in this section. Figure 2 shows channel spacing and resolving power for the AIRS L1c channel set [5]. The variable channel spacing and resolving power are due to the modular structure of the focal plane. Although

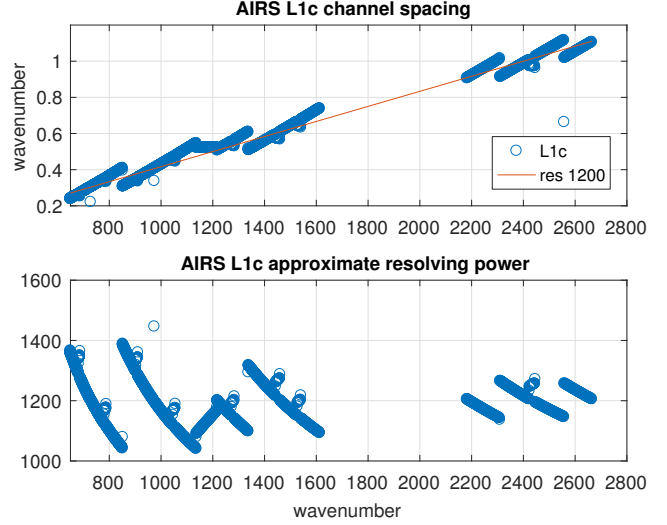


Figure 2: AIRS L1c channel spacing and resolving power,  $R = v_i/\text{FWHM}_i$ . The relatively regular L1c channel spacing aids the deconvolution.

not entirely regular—that is, not a simple function of frequency—the L1c channel set is more regular than the L1b channel set from which it is derived, and we mainly consider the L1c set here.

Suppose we have  $n$  channels and a frequency grid  $\vec{v}$  of  $k$  points spanning the union of the domains of the functions  $\sigma_i$ . The grid step size for our applications is often  $0.0025 \text{ cm}^{-1}$ , the default resolution for upwelling radiances calculated using the kCompressed Atmospheric Radiative Transfer Model (kCARTA) [12]. Let  $S_k$  be an  $n \times k$  array such that  $s_{i,j} = \sigma_i(v_j)/w_i$ , where  $w_i = \sum_j \sigma_i(v_j)$ , that is where row  $i$  is  $\sigma_i(v)$  tabulated at the grid  $\vec{v}$  and normalized so the row sum is 1. If the channel centers are in increasing order  $S_k$  is banded, and if they are not too close (as is the case for a few of the L1b channels) the rows are linearly independent.  $S_k$  is a linear transform whose domain is radiance at the grid  $\vec{v}$  and whose range is channel radiances. If  $r$  is radiance at the grid  $\vec{v}$ , then  $c = S_k r$  gives a good approximation of the channel radiances  $c_i = \int \sigma_i(v)r(v) dv$ . In practice this is how we calculate AIRS channel radiances for the validation tests described in subsequent sections.

For the AIRS to CrIS and other translations we are mainly interested in the transform  $S_b$  for SRFs at an intermediate resolution, typically  $0.1 \text{ cm}^{-1}$ . This is the approximate resolution of the SRF measurements and convenient for reconvolution to the CrIS user grid. So let  $\vec{v}_b = v_1, v_2, \dots, v_m$  be a  $0.1 \text{ cm}^{-1}$  grid spanning the domains of the functions  $\sigma_i$ . Similar to  $S_k$ , let  $S_b$  be an  $n \times m$  array where row  $i$  is  $\sigma_i(v)$  tabulated at the  $\vec{v}_b$  grid, with rows normalized to 1. If  $r$  is radiance at the  $\vec{v}_b$  grid, then  $c = S_b r$  is still a reasonable approximation of  $\int \sigma_i(v)r(v) dv$ .

For our application we want to start with  $c$  and find  $r$ , that is to deconvolve  $c$  by solving  $S_b r = c$  for  $r$ . Since  $n < m$ , the system is underdetermined. We take the Moore-Penrose pseudoinverse [8] of  $S_b$  to get  $r_0 = S_b^{-1} c$ . This gives a minimal solution, in the sense that  $\|r_0\|_2 \leq \|r_j\|_2$  for all  $r_j$  satisfying  $S_b r_j = c$ . The condition number for  $S_b$  as built from the L1c channels is  $\|S_b\|_2 \|S_b^{-1}\|_2 = 115$ , which is tolerable.

Although our main goal is to reconvolve the  $0.1 \text{ cm}^{-1}$  intermediate representation to the CrIS or other user grids, we first compare the deconvolved radiance with reference truth from a direct convolution of kCARTA radiance to the intermediate grid. The choice of response functions for the direct convolution is not obvious, since the deconvolution is undoing—at least to some extent—the effects of the AIRS SRF convolutions. We chose a generalized Gaussian [13] of the form

$$w(v, v_0, \text{FWHM}) = \exp \left( - \left( \frac{(v - v_0)^2}{2c^2} \right)^{1.5} \right)$$

where  $c = \text{FWHM} / (2\sqrt{2\ln 2})$  and  $v_0$  is the desired channel center. The exponent 1.5 was chosen to give an approximate match to AIRS SRFs with the same FWHM and channel centers, though without the fine structure and variation of the measured SRFs. Figure 1 shows two such generalized Gaussians paired with the corresponding AIRS SRFs. We used the generalized Gaussian as reference truth for the  $0.1 \text{ cm}^{-1}$  intermediate grid with  $\text{FWHM} = v_i / 2000$ , where  $v_i$  are the grid frequencies. This represents a hypothetical grating spectrometer with a resolving power of 2000, oversampled to the  $0.1 \text{ cm}^{-1}$  grid. The value of 2000 was chosen to give an approximate fit to the deconvolved radiances. We also tried a generalized Gaussian with a fixed FWHM for values 0.4, 0.6, and 0.8 and a sinc basis with a spacing of  $0.2 \text{ cm}^{-1}$ , all of which gave larger residuals.

The AIRS deconvolution gives a modest resolution enhancement, at the cost of added artifacts and noise. Figure 3 shows the full spectra from fitting profile 1, along with sample details from the low and high ends of the band, for the deconvolution and direct convolution to the intermediate grid. In the details we see some overshoot and ringing in the deconvolution. Figure 4 shows details of kCARTA, direct convolution to the  $0.1 \text{ cm}^{-1}$  grid, deconvolution, and AIRS spectra for fitting profile 1 [9, 10]. In the first subplot we see the deconvolution is capturing some of the fine structure in the kCARTA data that is present in the direct convolution but not in the AIRS data. In the second subplot we see the deconvolution (and direct convolution) resolving a pair of close lines that are not resolved at the AIRS L1c resolution. But we also see some ringing that is not present in the direct convolution. This is to be expected; significant

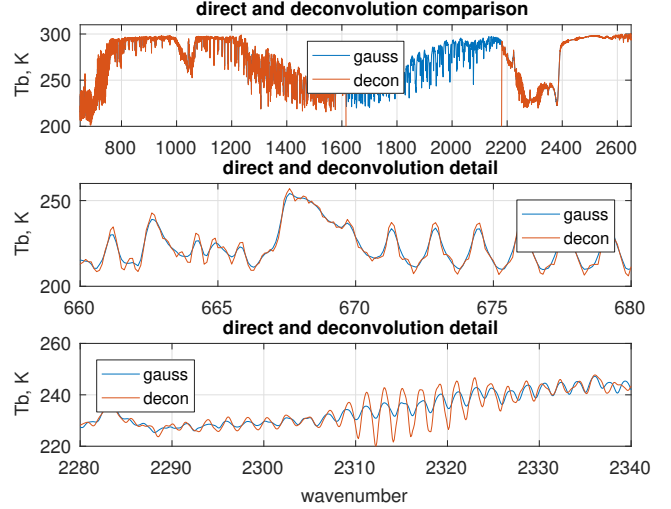


Figure 3: Spectra from fitting profile 1 for direct convolution to the  $0.1 \text{ cm}^{-1}$  grid and for deconvolved AIRS. We see some overshoot and ringing in the deconvolution.

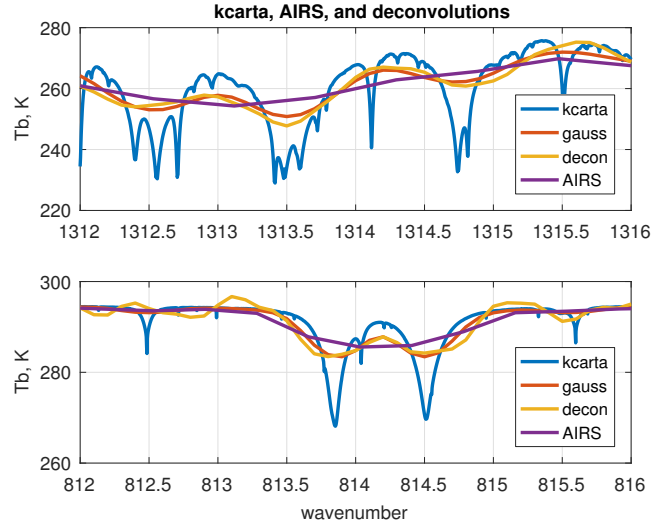


Figure 4: Details from fitting profile 1 for kCARTA, direct convolution to the  $0.1 \text{ cm}^{-1}$  grid, deconvolved AIRS, and true AIRS. The deconvolution restores some detail.

detail is lost in the convolution to AIRS channel radiances and this can only partially be recovered by the deconvolution. The artifacts are acceptable because we do not propose using the deconvolved radiances directly; they are an intermediate step before reconvolution to a lower resolution.

Figure 5 shows a pair of typical adjacent rows of the deconvolution matrix  $S_b^{-1}$  in the first subplot. Row  $i$  of  $S_b^{-1}$  is the weights applied to L1c channel radiances to synthesize the deconvolved radiance  $r_i$  at the intermediate grid frequency  $v_i$ . The oscillation shows we are taking the closest AIRS channel, subtracting weighted

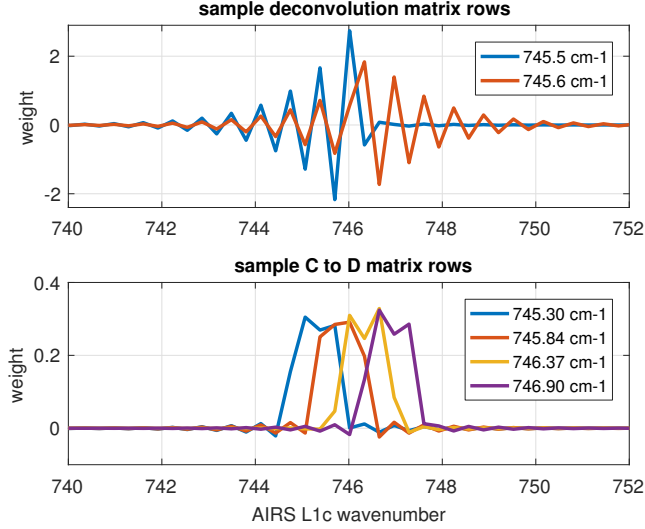


Figure 5: sample adjacent rows for the deconvolution and L1c to L1d transforms

values for channels  $\pm 1$  step away, adding weighted values for channels  $\pm 2$  steps away, and so on, with the weights decreasing quickly as we move away from  $v_i$ , with eight to ten L1c channels making a significant contribution to each deconvolution grid point. The second subplot shows four adjacent rows of the matrix  $S_d \cdot S_b^{-1}$ , which takes L1c to L1d channel radiances. (The L1d radiances are discussed in a later section; here they are of interest mainly as a typical reconversion.) Both matrices are banded but the bands are narrower in the second, with three to five L1c channels contributing significantly to each L1d channel. The range of influence is significant since we may want to know which L1d channels are derived in part from the synthetic L1c channels.

### 3 AIRS to CrIS translation

Given AIRS deconvolution to a  $0.1 \text{ cm}^{-1}$  intermediate grid, reconvolution to the CrIS user grid is straightforward. For CrIS standard resolution the channel spacing is  $0.625 \text{ cm}^{-1}$  for the LW band,  $1.25 \text{ cm}^{-1}$  for the MW, and  $2.5 \text{ cm}^{-1}$  for the SW. For each CrIS band, we (1) find the AIRS and CrIS band intersection, (2) apply a bandpass filter to the deconvolved AIRS radiances restricting them to the intersection, with a rolloff outside the passband, and (3) reconvolve the filtered spectra to the CrIS user grid with a zero-filled double Fourier transform [6]. The out-of-band rolloff smooths what would otherwise be an impulse at the band edges, reducing ringing in the translation.

Translations are tested by comparison with calculated reference truth. We start with a set of atmospheric profiles and calculate upwelling radiance at a  $0.0025 \text{ cm}^{-1}$

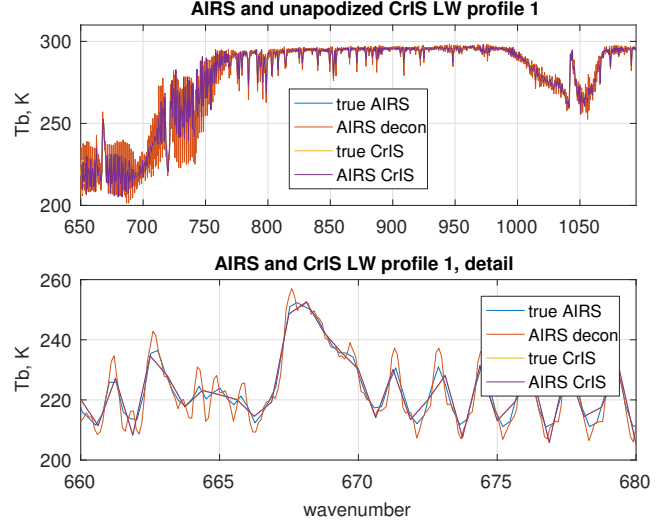


Figure 6: true AIRS, deconvolved AIRS, true CrIS, and AIRS CrIS. Differences between true CrIS and AIRS CrIS are too small to be visible in this figure.

grid with kCARTA [12] over a band spanning the domains of the AIRS and CrIS response functions. “True AIRS” is calculated by convolving the kCARTA radiances with AIRS SRFs and “true CrIS” by convolving kCARTA radiances to a sinc basis at the CrIS user grid. True AIRS is then translated to CrIS to get “AIRS CrIS”, and this is compared with true CrIS. Figure 6 shows sample spectra for true AIRS, deconvolved AIRS, true CrIS and AIRS CrIS. Any difference between true CrIS and AIRS CrIS is hard to see here, and in subsequent plots we mainly show explicit differences.

Comparisons are done both with and without apodization. Hamming apodization [14] sacrifices some resolution but gives a significant reduction in the residuals and is convenient for many applications. Convolution, deconvolution, and apodization are done with radiances, while spectra are presented and statistics are done after translation to brightness temperatures.

For most tests we use a set of 49 fitting profiles spanning a wide range of clear atmospheric conditions, initially chosen for testing radiative transfer codes [9, 10]. The set is largely uncorrelated; reducing the reconstruction residual to 0.02 K requires 48 left-singular vectors. (Details of this correlation measure are given in an appendix.) For the statistical correction described later in this section and the direct regression of section 5 we also use a set of 7377 radiances calculated from all-sky (clear and cloudy) AIRS profiles spanning several consecutive days. This set is more correlated; reducing the reconstruction residual to 0.02 K requires 260 left-singular vectors. Splitting the 7377 profile set into dependent and independent subsets and comparing residuals from the independent subset with residuals from the 49-profile set,

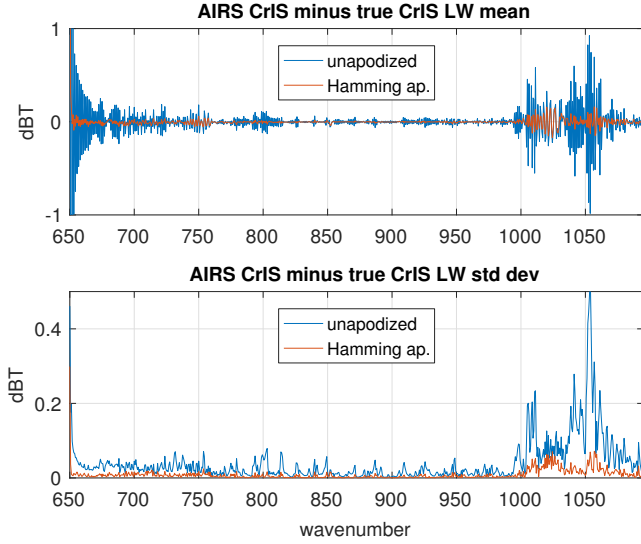


Figure 7: Mean and standard deviation of unapodized and Hamming apodized AIRS CrIS minus true CrIS, for the CrIS LW band

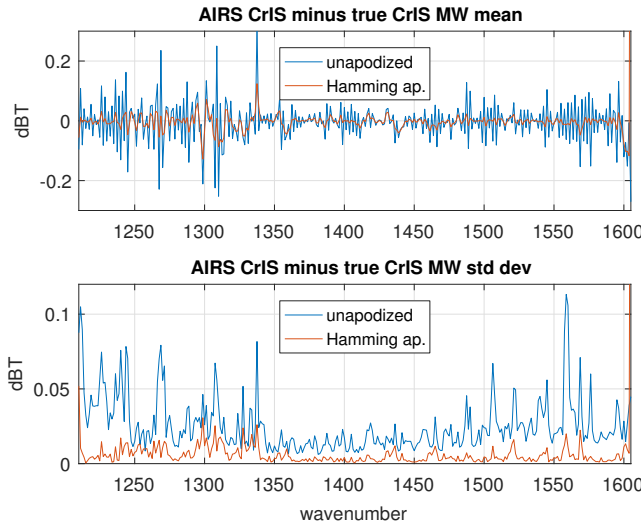


Figure 8: Mean and standard deviation of unapodized and Hamming apodized AIRS CrIS minus true CrIS, for the CrIS MW band.

residuals from the latter are consistently larger, suggesting it makes for a stricter test. So for the results shown here the test or independent set is always the 49-profile set, while for tests requiring fitting the 7377 profile is used as the dependent set.

Figures 7, 8, and 9 show the mean and standard deviation of true CrIS minus AIRS CrIS for the 49 fitting profiles, for each CrIS band. The Hamming apodization gives a significant reduction in the residuals. Figure 10 summarizes results all three bands, for apodized radiances. The constant or DC bias is very close to zero for the apodized residuals. The unapodized residuals are

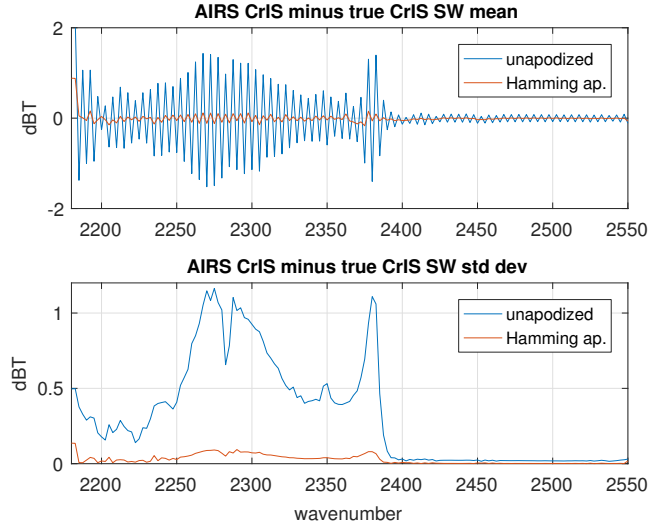


Figure 9: Mean and standard deviation of unapodized and Hamming apodized AIRS CrIS minus true CrIS, for the CrIS SW band.

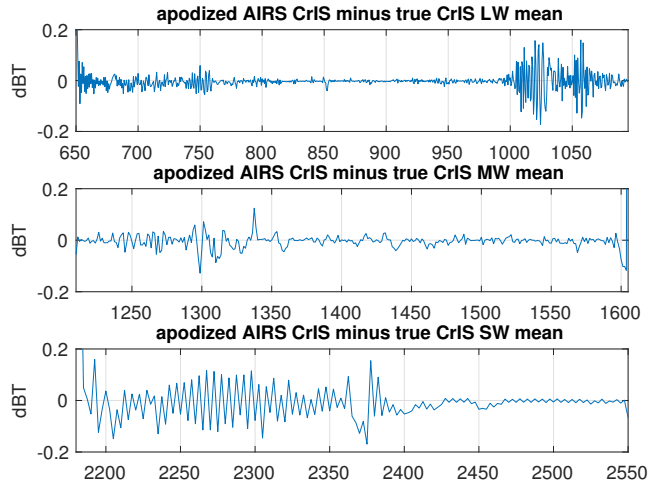


Figure 10: Mean of apodized residuals for all three CrIS bands, showing the residuals in greater detail.

significant but both the apodized and unapodized residuals are much less than the corresponding residuals from conventional interpolation, as shown in the appendix.

The relatively small standard deviation of the residuals suggests some regularity, and we can see an oscillation with a period of two channel steps in several places. Up to this point there has been no statistical component to our translation, beyond the choice of test set for validation. We feel it is important to be clear about any steps that require statistical fitting. That said, a simple linear correction can give a significantly further reduction of the residuals. We use the set of 7377 mostly cloudy AIRS profiles as the dependent set and the 49 profile set as the independent or test set.



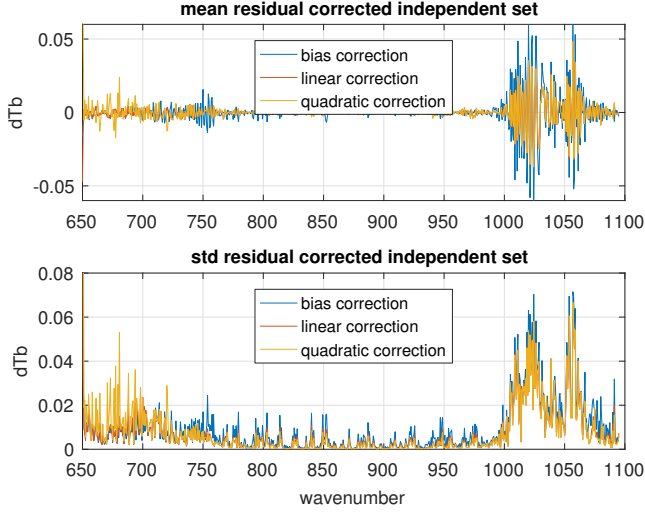


Figure 11: Mean and standard deviation of LW corrected apodized residuals

We compare three such corrections. These are done with a separate regression for each CrIS channel, and so introduce no cross-correlations. Let  $t_i^{\text{TC}}$  be true CrIS and  $t_i^{\text{AC}}$  AIRS CrIS brightness temperatures for CrIS channel  $i$ , from the dependent set. For the bias test we subtract the mean residual from the dependent set. For the linear test we find  $a_i$  and  $b_i$  to minimize  $\|a_i t_i^{\text{AC}} + b_i - t_i^{\text{TC}}\|_2$ , and for the quadratic test weights  $c_i$ ,  $a_i$  and  $b_i$  to minimize  $\|c_i (t_i^{\text{AC}})^2 + a_i t_i^{\text{AC}} + b_i - t_i^{\text{TC}}\|_2$ . The resulting correction is then applied to the independent set, the 49 fitting profiles, for comparison with true CrIS.

Figure 11 is a comparison of bias, linear, and quadratic corrections for the LW band. The linear and quadratic corrections are nearly identical, with the quadratic coefficient very close to zero. Figure 12 shows the weights for the linear fits from figure 11. The  $a$  weights are very close to 1 and the  $b$  weight to the bias. Figures 13 and 14 show the linear correction giving a similar improvement in the MW and a small improvement in the SW, where the quadratic correction is noticeably worse. Figure 15 shows the residuals for the apodized linear correction for all three bands. The residuals are significantly reduced in comparison with the apodized uncorrected radiances shown in figure 10.

We can give a good estimate of noise equivalent differential radiance (NEdN) for the translation by adding noise with a normal distribution at the AIRS NEdN to blackbody radiance at 280K and translating this to CrIS. This is done repeatedly and the noise after translation is measured. As a check, noise before translation is also measured and compared with the AIRS value. Figure 16 shows the measured AIRS-to-CrIS NEdN together with AIRS and CrIS NEdN for both apodized and unapodized radiances. The AIRS and CrIS values are averages over

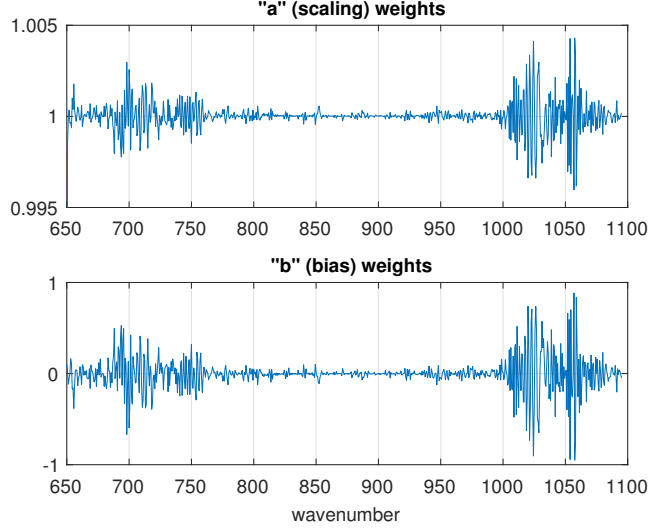


Figure 12: LW  $a$  and  $b$  weights for the linear correction  $ax + b$

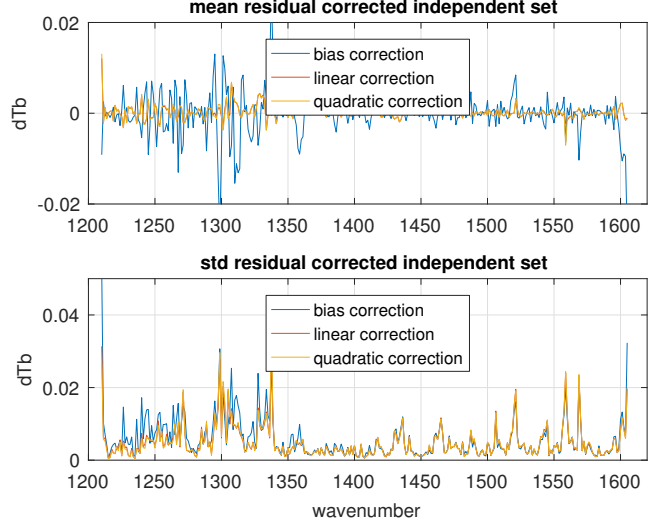


Figure 13: Mean and standard deviation of MW corrected apodized residuals.

a full day, 4 Dec 2016. NEdN for the L1c synthetic channels is interpolated. The first subplot of figure 17 is NEdT for apodized radiances, for fitting profile 1.

The AIRS channel-to-channel NEdN variation is significant; in the upper half of the LW and most of the MW it is of the same order as the AIRS and CrIS NEdN difference. This variation is due the AIRS focal plane structure and sensitivity. The AIRS and CrIS NEdN measures are both spiky when averaged over a few minutes but the CrIS variation is primarily uncertainty in the noise measurement and smooths out as the time span is extended, while the AIRS variation is stable. The AIRS-to-CrIS translation inherits this variability; it is a significant part of the difference between AIRS CrIS

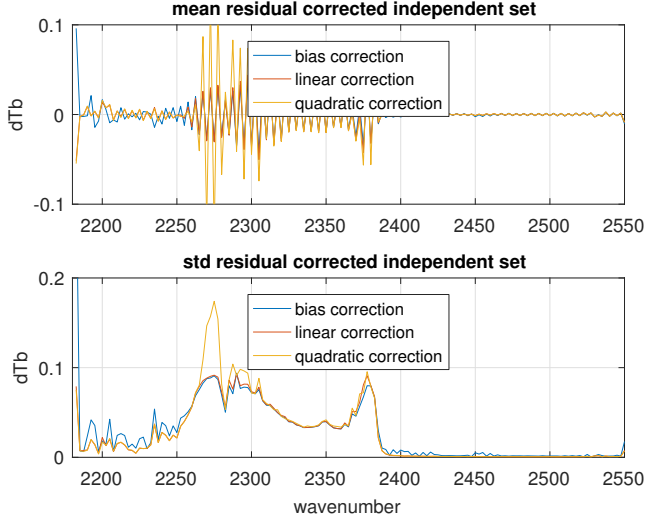


Figure 14: Mean and standard deviation of SW corrected apodized residuals.

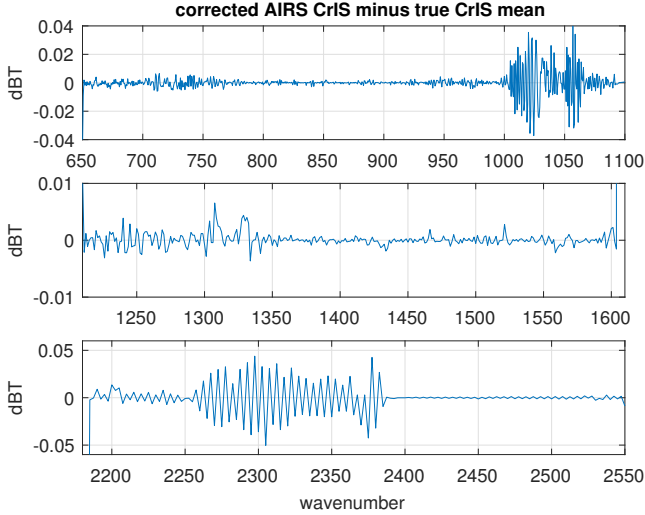


Figure 15: Mean corrected apodized residuals for all three bands, showing the linear corrected apodized residuals in greater detail.

and true CrIS. For a common record we might want to add noise on a channel-by-channel basis to whichever NEdN value—AIRS CrIS or true CrIS—is lower. NEdN for the combined record would then be max of the AIRS CrIS and true CrIS NEdN values, as shown in the second subplot of figure 17.

In addition to the standard resolution described at the beginning of this section, CrIS has a high resolution mode with a channel spacing of  $0.625 \text{ cm}^{-1}$  for all three bands. We can do a translation from AIRS to high-resolution CrIS but the residuals are quite large; AIRS does not have sufficient resolution as a starting point. The high resolution mode does allow for a CrIS to AIRS translation

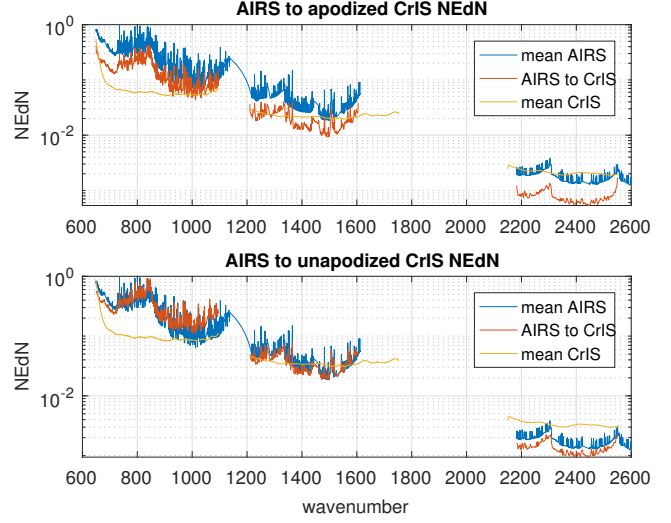


Figure 16: AIRS, AIRS-to-CrIS, and CrIS NEdN. Apodization reduces the CrIS and AIRS-to-CrIS NEdN by a factor of 0.63.

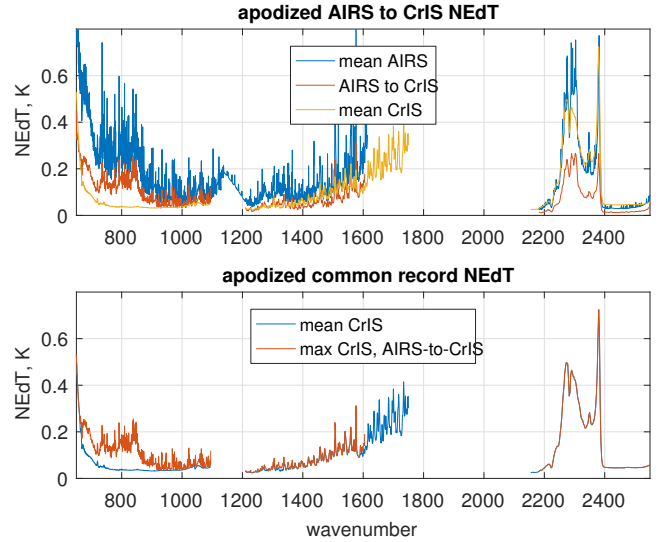


Figure 17: AIRS, AIRS-to-CrIS, and CrIS apodized NEdT, and the max of CrIS and AIRS-to-CrIS NEdN (shown as NEdT) with CrIS NEdT shown as a reference.

as described in [7]. The residuals are larger in the LW than for our translation from AIRS to standard resolution CrIS, but may be acceptable for some applications.

#### 4 Translation to an idealized grating model

The AIRS deconvolution can be used for other translations.

In this section we briefly examine reconvolution to an idealized grating model for resolving powers of 700 and

1200. There are several reasons to consider such a translation. The constant resolving power of the L1d basis (defined below) makes it a more natural translation target for AIRS than the constant channel spacing of CrIS. It could be considered as the next step in regularization of the AIRS product, following the partial regularization from L1b to L1c. If there were other operational hyperspectral grating spectrometers it would be a logical target for a common record.

Define an AIRS L1d basis with resolving power  $R$  using the generalized Gaussian response function of section 2 as follows. Let  $v_0$  be the frequency of the first channel and for  $i \geq 0$   $\text{FWHM}_i = v_i/R$ ,  $dv_i = \text{FWHM}_i/2$ , and  $v_{i+1} = v_i + dv_i$ . As with tests of the AIRS to CrIS translation, true L1c is calculated by convolving kCARTA radiances with AIRS L1c SRFs and true L1d by convolving with an L1d basis at the desired resolving power. L1c is translated to L1d by deconvolution followed by reconvolution to the desired L1d basis, and this is compared with true L1d.

Figure 18 shows residuals for reconvolution to an L1d basis with resolving power of 1200, the nominal AIRS resolution, and figure 19 shows residuals for a resolving power of 700. Note the different x-axes for the two figures. The residuals depend in part on the L1d starting channel  $v_0$ , and so on how the L1c and L1d SRF peaks line up. The residuals shown are the result of a rough fit for  $v_0$ . For a resolving power of 1200 this gave  $v_0$  equal to the first L1c channel, while for 700 it was the first L1c channel plus  $0.2 \text{ cm}^{-1}$ .

We see that for both the AIRS to CrIS and L1c to L1d translations some resolving power is sacrificed in shifting channel centers to a single regular function of frequency. Residuals for a resolving power of 1200 (figure 18) are roughly comparable to unapodized CrIS (figures 7, 8, and 9) and residuals for a resolving power of 700 (figure 19) are roughly comparable to apodized CrIS (figure 15). As with the AIRS to CrIS translation, the L1c to L1d residuals are significantly reduced with a linear correction. Residuals for L1d with a resolving power of 700 after correction are comparable to residuals for apodized CrIS after a similar correction.

## 5 Direct and principal component regression

The AIRS L1c to L1d translation can be done with a single linear transform  $S_d \cdot S_c^{-1}$ , where  $S_c$  and  $S_d$  are the transforms taking the intermediate grid to L1c and L1d channels. The AIRS to CrIS translation could also be done with a composite transform if we use a resampling matrix rather than double Fourier interpolation and a matrix form of the bandpass filters. We can get such a one-step transform in other ways. Suppose  $r_a$  and  $r_c$  are  $m \times k$  and  $n \times k$  AIRS and CrIS radiance sets, for

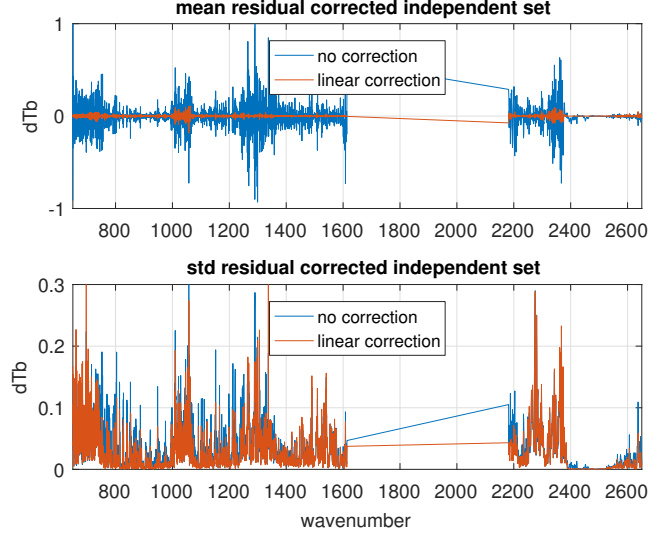


Figure 18: Mean and standard deviation over the 49 fitting profiles for the L1c to L1d translation minus true L1d for a resolving power of 1200.

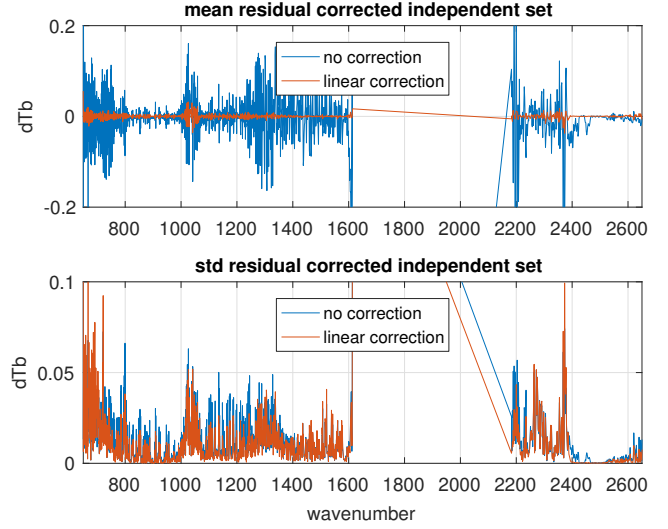


Figure 19: Mean and standard deviation over the 49 fitting profiles for the L1c to L1d translation minus true L1d for a resolving power of 700.

example true AIRS and true CrIS from section 3. We can find an  $n \times m$  matrix  $X$  by regression to minimize  $\|Xr_a - r_c\|_2$  and use this as our AIRS to CrIS transform. We call this standard technique “direct regression” here. This is different from the corrections of section 3 and 4; there regression was used to find linear or quadratic correction coefficients independently for each channel.

Figures 20 shows residuals for direct regression from AIRS to apodized CrIS radiances. As before we use the 7377 profile set as the dependent and the 49 profile as the independent set. The residuals are roughly compara-



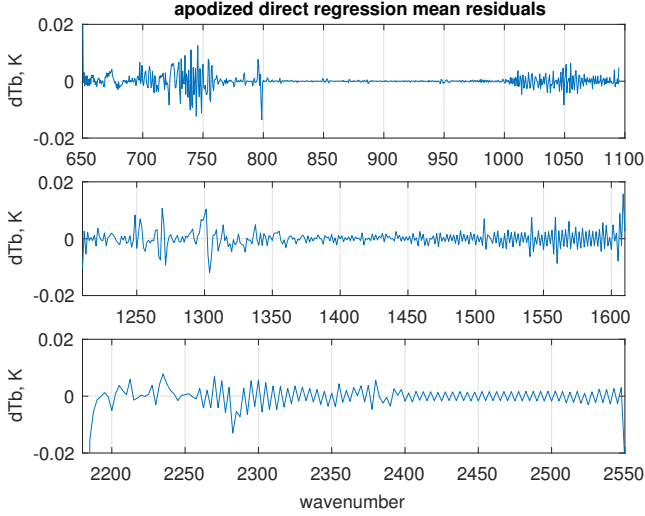


Figure 20: Mean residuals over the 49 profile independent set for AIRS to apodized CrIS direct regression.

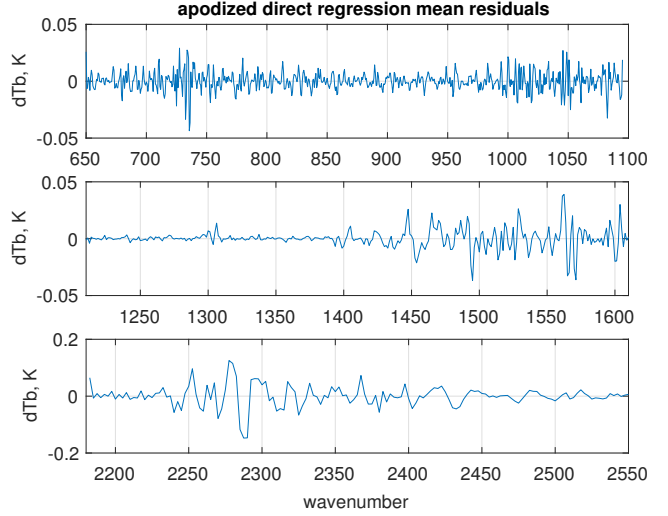


Figure 22: Mean residuals over the 49 profile independent set for AIRS to apodized CrIS principal component regression.

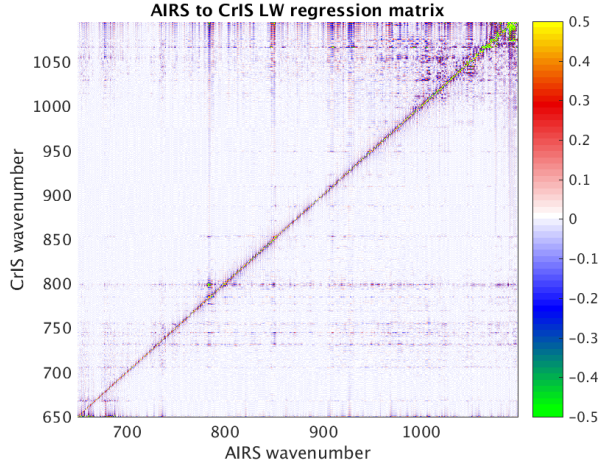


Figure 21: Regression coefficients from the 7377 profile dependent set for the LW direct regression.

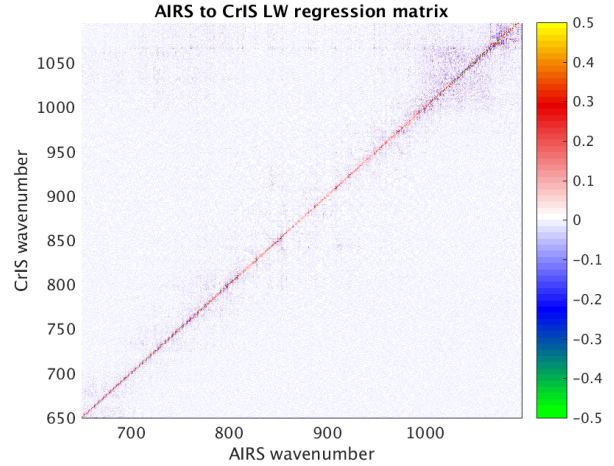


Figure 23: Regression coefficients from the 7377 profile dependent set for LW principal component regression with  $i = j = 500$ .

ble to the residuals from the deconvolution translation summarized in figure 15. However the regression matrices show significant off-diagonal correlations. Figure 21 shows this for the LW; the MW and SW bands are worse. In addition the dependent set residuals are very small, much less than the residuals for the independent set. These are signs of over-fitting. As noted in section 3 the 7377 profile dependent set is highly correlated; the effective dimension (as defined in the appendix) is only 260.

One fix is to add noise. Recall that we generate true AIRS and true CrIS by convolving a common set of high-resolution radiances. For true AIRS we can simply add noise at the AIRS NEdN. But for regression or testing of an AIRS to CrIS translation we want CrIS radiances with

actual translated AIRS noise, not simply true CrIS with noise added as per the CrIS NEdN specification. The latter does reduce correlations but increases residuals for the independent set significantly. To model NEdN for the AIRS to CrIS translation of section 3 we synthesize noise at the AIRS NEdN, add that to the signal, run signal plus noise through the translation, and measure the noise. But to get an AIRS to CrIS translation by regression with added noise we need a reference translation of each noisy AIRS spectra. We don't want to use the translation of section 3 for that, at least not if our goal is to give each translation method an independent test.

As an alternative to adding noise, we can use a form of principal component regression. As above, let  $r_a$  and

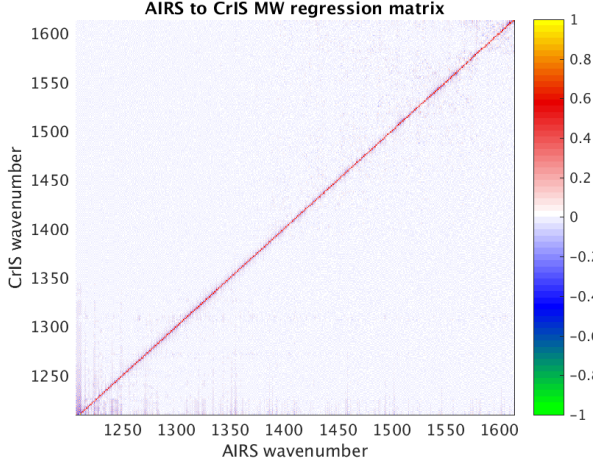


Figure 24: Regression coefficients from the 7377 profile dependent set for MW principal component regression with  $i = 500$  and  $j = 320$ .

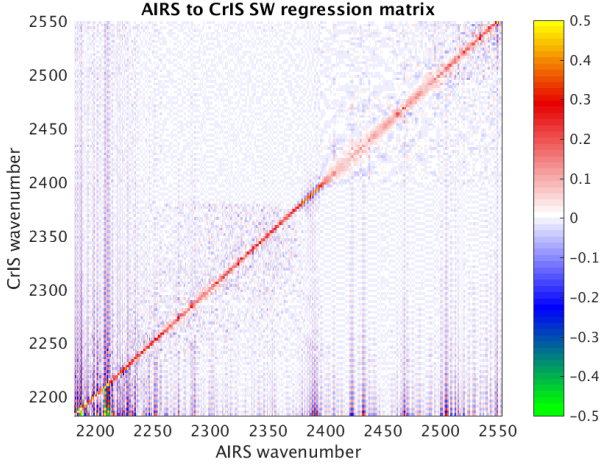


Figure 25: Regression coefficients from the 7377 profile dependent set for SW principal component regression with  $i = j = 100$ .

$r_c$  be  $m \times k$  and  $n \times k$  AIRS and CrIS radiance sets. Let  $r_a = U_a S_a V_a^T$  be the singular value decomposition with singular values in descending order and  $U_a^i$  the first  $i$  columns of  $U_a$ . Similarly let  $r_c = U_c S_c V_c^T$  be a singular value decomposition with singular values in descending order and  $U_c^j$  the first  $j$  columns of  $U_c$ . Let  $\hat{r}_a = (U_a^i)^T r_a$  and  $\hat{r}_c = (U_c^j)^T r_c$  be  $r_a$  and  $r_c$  represented with respect to the bases  $U_a^i$  and  $U_c^j$ . (Since the bases are orthonormal, the transpose is the inverse.) Then as before find  $X$  by regression to minimize  $\|X\hat{r}_a - \hat{r}_c\|_2$ . This gives us  $R = U_c^j X (U_a^i)^T$ , an AIRS to CrIS transform parameterized by the basis sizes  $i$  and  $j$ .

Note that this sort of principal component regression is not the same as regression after principal component (or singular vector) filtering; for that we would take

$\bar{r}_a = U_a^i (U_a^i)^T r_a$ ,  $\bar{r}_c = U_c^j (U_c^j)^T r_c$ , find  $X$  to minimize  $\|X\bar{r}_a - \bar{r}_c\|_2$ , and have no need for a change of bases to apply  $X$ . In practice this did not work as well as doing regression after the change of bases.

Figure 22 shows residuals and figures 23, 24, and 25 the transform  $R$  for the CrIS LW, MW, and SW bands. We have chosen  $i = j = 500$  for the LW,  $i = 500$  and  $j = 320$  for the MW, and  $i = j = 100$  for the SW for the basis sizes, to roughly balance unwanted correlation with residual size. The residuals for principal component regression are larger than for the deconvolution translation with regression correction and there is still significant off-diagonal correlation, especially for the MW and SW bands.

## 6 Applications

We have been using the AIRS to CrIS and IASI to CrIS translations to analyze simultaneous nadir overpasses (SNOs) [3]. We hope to create a long-term climate record spanning observations of the individual sounders. The initial steps are validation with SNOs, validation of uniform geographic sampling and subsetting, and showing consistency of global statistics. Radiance translation to a common subset might include added noise, as discussed in section 3. The radiance translations could be explicit or implicit—that is, run once and saved as a dataset, or run as needed on existing data. Translations are fast relative to read times.

The translations allows a retrieval algorithm to use the same fast forward radiative transfer model, minimizing any differential effect of forward model errors between the two instrument retrievals. An interesting potential application is to revisit the AIRS SRF measurements, to see if adjustments (within the original measurement uncertainty) can reduce the translation residuals.

The translations presented here have been implemented and tested extensively, with the associated Matlab code published on Github. The AIRS to CrIS translation is I/O bound, with the in-core time divided into roughly 25 percent for the deconvolution and 75 percent for reconvolution, taking about 22 seconds to process our 7377 profile cloudy test set on one compute node. Calculating the pseudo-inverse adds another 12 seconds, but that only needs to be done when the translation parameters change.

## 7 Appendix

### 7.1 Measures of correlation

We want to measure the correlation of a set of radiances. One such measure is dimension of a spanning set. For an

approximation we use the basis size needed to get reconstruction residuals below some fixed threshold. Let  $r_0$  be an  $m \times n$  array of radiances, one row per channel and one column per observation. Let  $r_1 = USV^T$  be a singular value decomposition with singular values in descending order and  $U_k$  the first  $k$  columns of  $U$ . Let  $r_k = U_k U_k^T r_0$ ; then  $r_k \approx r_0$ . The approximation improves as  $k$  increases and becomes exact for some  $k \leq m$ . This is the analog of principal component filtering using left-singular rather than eigenvectors and is useful as a form of compression when  $k$  is small relative to  $n$ . For that case we save  $U_k$  and  $U_k^T r_0$  separately. Applications include compression of IASI radiance data and the kCARTA absorption coefficient database.

We use a threshold for equivalence that is relevant for our applications. Let  $B^{-1}$  be the inverse Planck function and define  $d(r_1, r_2) = \text{RMS}(B^{-1}(r_1, v) - B^{-1}(r_2, v))$ , the RMS difference over all channels and observations of the brightness temperatures of radiance data. Finally let  $j$  be the smallest value such that  $d(r_0, r_j) \leq T_d$ , for some threshold  $T_d$ . Then  $j$  is the effective dimension of our set  $r_0$ . Here we have chosen  $T_d = 0.02$  K. For the 49 profile fitting set this gives  $j = 48$ , which we interpret as largely uncorrelated, while for the 7377 profile cloudy set we found  $j = 260$ , which we interpret as highly correlated.

## 7.2 Conventional interpolation

The AIRS to CrIS translation via deconvolution works significantly better than conventional interpolation. We consider two cases. For the first, start with true AIRS and interpolate radiances directly to the CrIS user grid with a cubic spline. For the second, interpolate true AIRS to the  $0.1 \text{ cm}^{-1}$  intermediate grid with a cubic spline and then convolve this to the use CrIS user grid. Figure 26 shows interpolated CrIS minus true CrIS for the LW band, without apodization. The two-step interpolation works a little better than the simple spline, but both residuals are significantly larger than for the translation with deconvolution. Results for the MW are similar, while the unapodized comparison is less clear for the SW. With Hamming apodization, the residuals with deconvolution are significantly less than interpolation for all three bands.

For the AIRS L1c to L1d translation, deconvolution again works significantly better than interpolation. As before, we consider two cases. For the first, start with true AIRS and interpolate radiances directly to the L1d grid with a cubic spline. For the second, interpolate true L1c to the  $0.1 \text{ cm}^{-1}$  intermediate grid with a cubic spline and convolve this to the L1d channel set. Figure 27 shows interpolated L1d minus true L1d, for a resolving power of 700. The two-step interpolation works a little

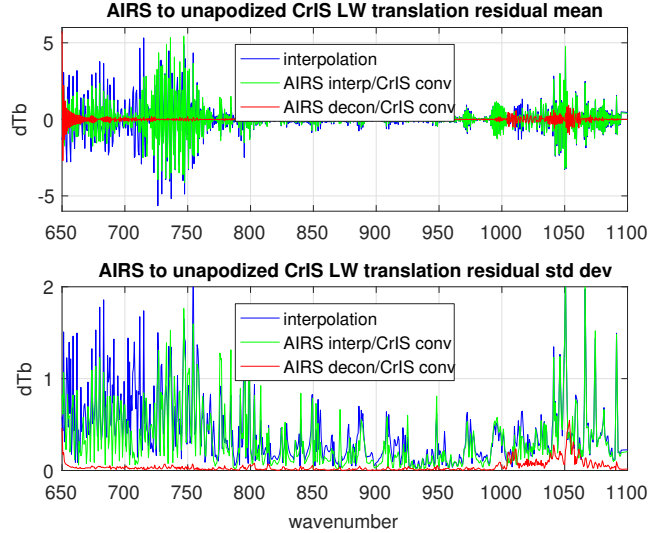


Figure 26: spline interpolation, interpolation with convolution, and deconvolution with convolution for the CrIS LW band.

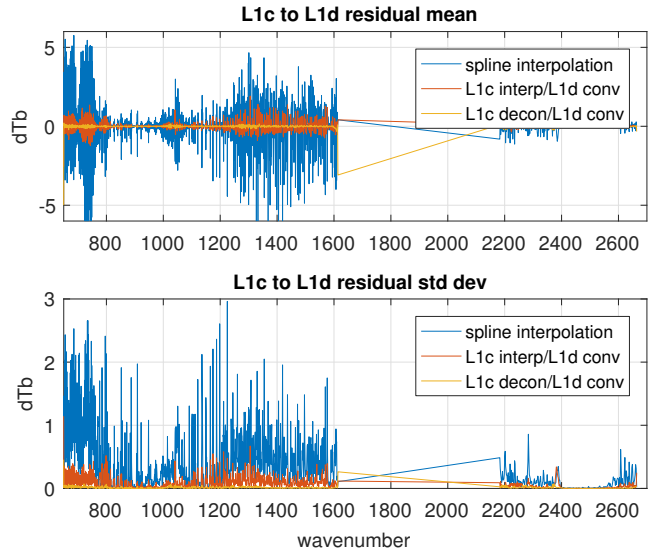


Figure 27: spline interpolation, interpolation with convolution, and deconvolution with convolution for the AIRS L1c to L1d translation with  $v_0 = 649.822 \text{ cm}^{-1}$  and a resolving power of 700

better than the simple spline, but is still much larger than the residual for translation with deconvolution.

## 7.3 Source code

All translation and test code discussed here is available online at Github:

- [https://github.com/strow/airs\\_deconv](https://github.com/strow/airs_deconv)
- [https://github.com/strow/iasi\\_decon](https://github.com/strow/iasi_decon)

## References

- [1] H. H. Aumann, M. T. Chahine, C. Gautier, M. D. Goldberg, E. Kalnay, L. M. McMillin, H. Revercomb, P. W. Rosenkranz, W. L. Smith, D. H. Staelin, L. L. Strow, and J. Susskind. AIRS/AMSU/HSB on the aqua mission: design, science objectives, data products, and processing systems. *IEEE Transactions on Geoscience and Remote Sensing*, 41:253–264, Feb. 2003.
- [2] Y. Han, H. Revercomb, M. Crompt, D. Gu, D. Johnson, D. Mooney, D. Scott, L. Strow, G. Bingham, L. Borg, Y. Chen, D. DeSlover, M. Esplin, D. Hagan, X. Jin, R. Knuteson, H. Motteler, J. Predina, L. Suwinski, J. Taylor, D. Tobin, D. Tremblay, C. Wang, L. Wang, L. Wang, and V. Zavyalov. Suomi NPP CrIS measurements, sensor data record algorithm, calibration and validation activities, and record data quality. *Journal of Geophysical Research (Atmospheres)*, 118(D17):12734, Nov. 2013.
- [3] C. Hepplewhite and L. L. Strow. A Hyper-Spectral Multi-Sensor Infrared Radiance Data Record for Climate Trending: Validation using Simultaneous Nadir Observations. In preparation, UMBC/JCET, 2017.
- [4] F. Hilton, R. Armante, T. August, C. Barnett, A. Bouchard, C. Camy-Peyret, V. Capelle, L. Clarisse, C. Clerbaux, P.-F. Coheur, A. Collard, C. Crevoisier, G. Dufour, D. Edwards, F. Fajtan, N. Fourrié, A. Gambacorta, M. Goldberg, V. Guidard, D. Hurtmans, S. Illingworth, N. Jacquinet-Husson, T. Kerzenmacher, D. Klaes, L. Lavanant, G. Masiello, M. Matricardi, A. McNally, S. Newman, E. Pavelin, S. Payan, E. Péquignot, S. Peyridieu, T. Phulpin, J. Remedios, P. Schlüssel, C. Serio, L. Strow, C. Stubenrauch, J. Taylor, D. Tobin, W. Wolf, and D. Zhou. Hyper-spectral Earth Observation from IASI: Five Years of Accomplishments. *Bulletin of the American Meteorological Society*, 93:347–370, Mar. 2012.
- [5] E. M. Manning, H. H. Aumann, D. A. Elliott, and L. L. Strow. AIRS Level 1C Algorithm Theoretical Basis. Version 3.0, Jet Propulsion Laboratory, Jan. 2015.
- [6] H. E. Motteler and L. L. Strow. Interferometric Interpolation. [https://github.com/strow/airs\\_deconv/blob/master/doc/finterp.pdf](https://github.com/strow/airs_deconv/blob/master/doc/finterp.pdf), 2014.
- [7] H. E. Motteler and L. L. Strow. Deconvolution and translation between high spectral resolution IR sounders. [https://github.com/strow/airs\\_deconv/blob/master/doc/decon\\_atbd.pdf](https://github.com/strow/airs_deconv/blob/master/doc/decon_atbd.pdf), 2016.
- [8] G. Strang. *Linear Algebra and Its Applications*. Academic Press, second edition, 1980.
- [9] L. Strow, S. Hannon, S. De Souza-Machado, H. Motteler, and D. Tobin. An overview of the airs radiative transfer model. *Geoscience and Remote Sensing, IEEE Transactions on*, 41(2):303–313, Feb 2003.
- [10] L. L. Strow, S. E. Hannon, S. De-Souza Machado, H. E. Motteler, and D. C. Tobin. Validation of the atmospheric infrared sounder radiative transfer algorithm. *Journal of Geophysical Research: Atmospheres*, 111(D9), 2006. D09S06.
- [11] L. L. Strow, H. Motteler, D. Tobin, H. Revercomb, S. Hannon, H. Buijs, J. Predina, L. Suwinski, and R. Glumb. Spectral calibration and validation of the Cross-track Infrared Sounder on the Suomi NPP satellite. *Journal of Geophysical Research (Atmospheres)*, 118(D17):12486, Nov. 2013.
- [12] L. L. Strow, H. E. Motteler, R. G. Benson, S. E. Hannon, and S. D. Souza-Machado. Fast computation of monochromatic infrared atmospheric transmittances using compressed look-up tables. *Journal of Quantitative Spectroscopy and Radiative Transfer*, 59(3 - 5):481 – 493, 1998. Atmospheric Spectroscopy Applications 96.
- [13] Wikipedia contributors. Gaussian function. [https://en.wikipedia.org/wiki/Gaussian\\_function](https://en.wikipedia.org/wiki/Gaussian_function). Accessed 12 Nov 2017.
- [14] Wikipedia contributors. Window function. [https://en.wikipedia.org/w/index.php?title=Window\\_function](https://en.wikipedia.org/w/index.php?title=Window_function). Accessed 12 Nov 2017.